Taylor & Francis
Taylor & Francis Group

Mechanics of Advanced Materials and Structures

ISSN: 1537-6494 (Print) 1537-6532 (Online) Journal homepage: www.tandfonline.com/journals/umcm20

Time domain analysis of locally resonant elastic metamaterials under impact*

Erdem Caliskan , Willoughby Cheney , Weidi Wang , Thomas Plaisted , Alireza V. Amirkhizi & Reza Abedi

To cite this article: Erdem Caliskan , Willoughby Cheney , Weidi Wang , Thomas Plaisted , Alireza V. Amirkhizi & Reza Abedi (2026) Time domain analysis of locally resonant elastic metamaterials under impact*, Mechanics of Advanced Materials and Structures, 33:1, 2619034, DOI: 10.1080/15376494.2026.2619034

To link to this article: https://doi.org/10.1080/15376494.2026.2619034

MECHANICS OF ADVANCED MATERIALS AND STRUCTURES
2026, VOL. 33, NO. 1, 2619034
https://doi.org/10.1080/15376494.2026.2619034

Taylor & Francis
Taylor & Francis Group

ORIGINAL ARTICLE

Time domain analysis of locally resonant elastic metamaterials under impact*

Erdem Caliskan[a], Willoughby Cheney[b], Weidi Wang[b], Thomas Plaisted[c], Alireza V. Amirkhizi[b], and Reza Abedi[a]

[a]Department of Mechanical, Aerospace and Biomedical Engineering, University of Tennessee Knoxville, Knoxville, TN, USA; [b]Department of Mechanical Engineering, University of Massachusetts Lowell, Lowell, MA, USA; [c]DEVCOM Army Research Laboratory, Aberdeen Proving Ground, Aberdeen, MD, USA

ABSTRACT

Impact mitigation using metamaterials (MM) requires low-frequency stopbands for wave attenuation. Conventional low-frequency MM solutions often rely on complex, heavy, multi-material unit cells. Most MM studies analyze infinite periodic domains through *Frequency Domain* (FD) simulations, a practice that limits applicability to realistic impact scenarios. The present study employs *Time Domain* (TD) finite element analysis to investigate the dynamic response of single-material, locally resonant ceramic MMs under impact loading. This design achieves a low-frequency stopband while minimizing the mass and fabrication complexity associated with multi-material systems. TD results are contrasted with FD predictions to highlight the advantages of TD analysis for finite-sized structures subjected to impact, blast, and other boundary conditions. MM slabs are benchmarked against conventional monolithic and alternative microstructured slabs, with performance assessed in terms of stress-wave attenuation, peak-load retardation, energy transfer, and dissipation by material damping. Resonance within the MM amplifies dissipation within the assumed mass-proportional Rayleigh damping model. A graded slab further enhances energy mitigation by broadening the attenuation band relative to uniform MM slabs. Overall, the proposed MM design slows and redistributes stress waves, and the TD analysis framework provides a robust, efficient tool for such structures.

ARTICLE HISTORY
Received 26 April 2025
Accepted 5 January 2026

KEYWORDS
Energy mitigation; impact; wave propagation; mechanical metamaterial; blast

1. Introduction

The dynamic properties of materials depend significantly on their microstructure. Metamaterials (MMs) are engineered structures with microstructures that possess properties not found in nature. Dynamic mechanical MMs can interact with stress waves in unprecedented ways, providing control over wave trajectory and dissipation characteristics [1]. These materials find applications across diverse fields, including blast protection [2–4], acoustic wave mitigation [5–7], seismic shielding [8,9], and lenses [10]. Elastic and acoustic MMs can exhibit exotic mechanical properties, including frequency-dependent (dispersive) behavior and even negative effective mass density [11,12] or elastic moduli [10,13]. These exotic properties enable MMs to achieve superior performance compared to traditional designs in elastic wave mitigation [14–20].

Two primary mechanisms create bandgaps (frequency ranges where infinitely periodic structures prohibit wave propagation [21]): Bragg scattering and local resonance [22]. Bragg scattering bandgaps arise from structural symmetry, periodicity, and order [23,24]. However, their frequencies remain limited to approximately c/a, where c is the wave speed and a is the lattice constant [25]. This constraint makes Bragg scattering unsuitable for mechanical MMs since long wavelengths require large structures [26,27]. In contrast, locally resonant MMs can reduce bandgap frequencies by several orders of magnitude since they are governed by unit cell resonance frequencies rather than wavelength-lattice spacing relationships [28,29]. This advantage makes locally resonant designs attractive for mechanical wave control applications.

Graded designs can further enhance locally resonant MM arrays [30–33], which do not require perfect periodicity. Researchers can modify the wave speed profile of finite arrays by adjusting material properties or geometry at the unit cell level [34]. This approach enables slabs (one-dimensional arrays with periodicity in perpendicular directions) to operate effectively across wider frequency ranges and dissipate more energy. Locally resonant materials can also exhibit "metadamping" or "damping emergence," significantly enhancing shock absorption capabilities [35,36]. Additionally, damping inclusion resolves inherent ambiguities in the dynamic properties of lossless materials by providing physically meaningful solutions [37].

CONTACT Reza Abedi rabedi@utk.edu Department of Mechanical, Aerospace and Biomedical Engineering, University of Tennessee Knoxville, 1506 Middle Drive, Knoxville, 37916, TN, USA.
*Distribution Statement A.
Approved for public release: distribution is unlimited.
Supplemental data for this article can be accessed online at https://doi.org/10.1080/15376494.2026.2619034.

Current MM implementations face several critical limitations. Metaconcrete, an early locally resonant MM application, demonstrated potential for blast-wave mitigation [38–40], but suffers from key weaknesses: (1) it targets blast rather than ballistic/impact loading, (2) it requires compliant coating materials that compromise mechanical integrity, (3) researchers have not verified of critical mechanisms like friction and pounding in multi-material designs [41], and (4) it exhibits excessive weight for most applications. Recent hybrid MM designs combining local resonance with negative Poisson's ratio features [42,43] primarily focus on *Frequency Domain* (FD) analysis and experimental slab investigations, neglecting projectile impact scenarios and *Time Domain* (TD) analysis of realistic finite structures.

While FD analysis provides valuable insights into infinite periodic structures, TD analysis of finite MMs offers crucial advantages for practical applications. TD simulations enable realistic impact analysis by capturing transient wave interactions, energy dissipation mechanisms, and boundary effects that govern real-world performance. Unlike FD approaches, which assume infinite periodicity, TD analysis accounts for finite-size effects, loading duration, and complex wave reflections within bounded structures. This approach provides direct evaluation of energy mitigation performance under actual impact conditions, yielding insights essential for engineering applications.

Researchers have proposed a promising H-shaped resonator design for impact mitigation, potentially addressing the limitations of metaconcrete [44]. This design targets additive manufacturing using high-strength materials such as ceramics, featuring seamless transitions from enclosure to resonator that enhance structural integrity. The monolithic microstructured design protects internal structures from direct projectile interaction [45]. Furthermore, researchers can optimize bandgaps for ballistic and impact events at low frequencies through the oscillatory resonator's low natural frequency. Recent computational advances have enabled the efficient analysis of this topology, with reduced-order models (ROMs) achieving high accuracy in both eigenfrequency and TD computations [46]. Optimization studies using genetic algorithms with ROMs have demonstrated successful bandgap tuning through thickness-graded slab designs [47].

This work systematically investigates H-cell MMs through comprehensive TD analysis of finite arrays, providing several key innovations: (1) lightweight single-material design achieving low-frequency stopbands with enhanced stress-wave control, (2) systematic TD analysis revealing realistic impact performance and finite-size effects, (3) demonstration of multiplicative energy dissipation enhancement with material damping within the assumed mass-proportional Rayleigh damping model, (4) graded MM slab designs enabling broadband mitigation and improved peak load retardation, and (5) comprehensive evaluation of boundary conditions and loading scenarios on MM performance.

The investigation encompasses slab size effects, boundary condition influences, and various loading conditions, including projectile and blast scenarios. By expanding analysis beyond lossless structures, this study demonstrates that MMs induce multiplicative increases in energy dissipation as material damping increases when using the mass-proportional Rayleigh damping model. Through grading the MM slab, this work achieves broadband mitigation over extended frequency ranges, effectively improving peak load retardation and energy transfer compared to uniform designs. This MM can be manufactured into lightweight, graded protective panels or liners for vehicles and aerospace structures.

This study employs linear material models and does not account for nonlinear effects such as fracture, plasticity, or large deformation. The analysis assumes elastic wave propagation and does not consider material degradation or contact nonlinearities that may occur under extreme loading conditions. These simplifications enable systematic investigation of fundamental MM behavior while providing a foundation for future nonlinear studies.

2. Material and methods

This section details the approach for evaluating the performance of different designs through finite element simulations. The section begins by describing the material properties and geometry of the resonant metamaterial design, along with three comparison configurations used to benchmark performance. The analysis then outlines the computational methods, boundary conditions, and loading scenarios used in the investigation. Finally, the section defines the quantitative metrics employed to evaluate wave propagation and energy dissipation characteristics across different designs.

The material for the MM is alumina with a density of 3985 kg/m^3 [48], the elastic modulus of 300 GPa, and Poisson's ratio of 0.27 [49]. Additive manufacturing can be used to print a target microstructural design. The density of the material is taken from an additive manufacturing supplier, but the mechanical properties are taken from common alumina, since they are not provided by the supplier. The bandgap of the unit cell has been tuned between 20 and 40 kHz frequency range, which is illustrated in Figure 3b.

The geometry of the square MM design is given in Figure 1a. The resonator is H-shaped and connected to the frame from the middle horizontal line on the top and bottom sides. The area of the unit cell is 10 mm × 10 mm, while the wall, web, gap, and H-head dimensions are 0.5, 0.9, 0.25, and 3.875 mm, respectively. Three other candidate geometries are selected for comparison: monolithic, equal gap, and square cavity, shown in Figures 1b, 1c, and 1d, respectively. All comparison cells have the same outer dimensions, while the equal gap and square cavity also have the same mass as the H-cell MM. The monolithic cell represents the conventional design for protection. On the other hand, the equal gap is designed to have the same section area for stress waves to travel, while the square cavity is a simple cell design with the same mass. Long-wavelength wave speeds (c, based on overall density and quasi-static modulus) for these unit cell designs are provided in Table 1.

This study conducts computational experiments using LS-DYNA [50]. A Python script using the LASSO and qd libraries [51,52] performs postprocessing of the results. The

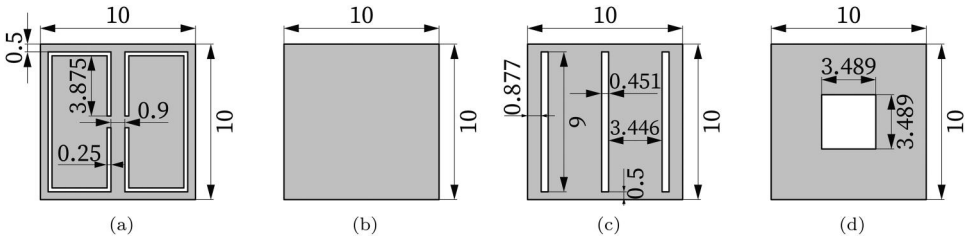

Figure 1. Unit cells used in this study: (a) resonant MM cell, (b) monolithic cell, (c) same mass with equal stress path gap, and (d) same mass with a square cavity.

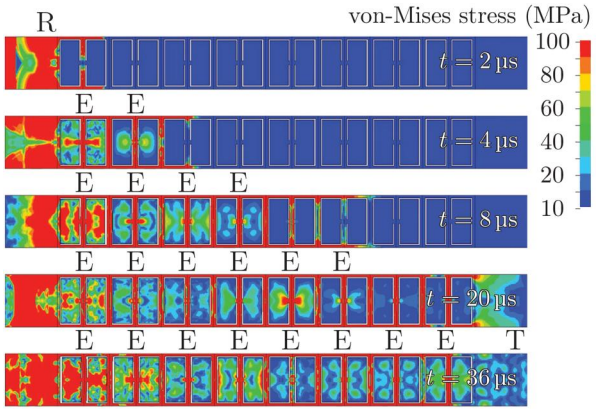

Figure 2. Snapshots of the von-Mises stress plotted on the array at five different timesteps. Reflection (R), resonator engagement (E), and transmission (T) have been annotated in the figure.

structure is meshed with uniform quadrilateral elements with a size of 0.025 mm. This element size is selected since it provides a mesh with equally sized square elements throughout the domain while being able to resolve the longitudinal waves (wave speed for the MM is provided in Table 1) at 40 kHz with around 150 elements per wavelength. In addition, the change in the energy transfer from 0.025 mm-sized mesh to 0.0125 mm-sized mesh is less than 0.5%; thus, 0.025 mm elements have been used for the remainder of this study.

For the projectile impact (PI) simulations, the material is selected as cold-rolled steel, with a density, Young's modulus, and Poisson's ratio of 7980 kg/m^3, 200 GPa, and 0.3, respectively [53]. Contact between the projectile and the ceramic slab is modeled using the mortar contact algorithm. Possible contacts within the unit cell are also tracked, although no such contact has been detected in the simulations conducted in this study. Energy transfer across the interface is calculated by integrating the power over time, and the TD results are turned into FD by using the Fourier transform, which is explained in detail in Appendix A.

Idealized boundary conditions, such as prescribed traction (PT) and prescribed velocity (PV), can be used to represent the two extremes of the impedances at the loaded front face; PT would provide more energy to the slab with a lower effective impedance, as the traction is provided from the PT boundary condition, whereas the corresponding normal velocity increases inversely proportional to the impedance. Since an MM slab has a lower impedance than a monolithic slab, it may be observed to have several times higher energy transfer from the PT boundary condition. Yet, under PV, the opposite holds true. Nevertheless, modeling

Table 1. Long wavelength wave speed (c) for the unit cells.

Unit cell	c (m/s)
MM	2951
Monolithic	8677
Equal gap	3788
Square gap	8603

the PI condition best represents actual impact scenarios, and blast loading (discussed below) is also a typical loading condition for these applications [38].

For the PI, the projectile length influences the time scale of the loading. While the default projectile length is $l_p = 20$ mm, when the effect of loading time scale is examined, the projectile length of $l_p = 2.5$ mm is also considered. A square pulse profile is used for PT and PV loadings. The duration of the square pulse t_d takes the value of 25 μs. Finally, the modified Friedlander approximation [38] is used to represent blast loading, where the time scale t_d takes the same value used for square pulse PT and PV boundary conditions. Since the material response is assumed to be linear in this study, the loading amplitude is of secondary importance. This analysis employs $v_0 = 30$ m/s for the PI loading. This results in an initial normal traction of 600 MPa. The load amplitudes for the PT, PV, and blast loadings are chosen to result in the same initial normal traction value.

This study is strictly linear elastic. Real impact/blast dissipation in ceramics is dominated by fracture, fragmentation, microcracking, and inelastic crushing, which are highly nonlinear phenomena and not captured in this work. Consequently, absolute energy transfer values should not be interpreted as predictive of survivability under severe impact; the present results isolate wave scattering, slowdown, and small-strain damping. The primary role of the linear study is to quantify how the architecture propagates stress waves prior to the onset of nonlinear failure. Establishing protective value requires nonlinear damage modeling and experiments on additively manufactured alumina, which are identified as essential next steps.

3. Results and discussion

This section systematically examines the performance of locally resonant metamaterial slabs under various conditions. The analysis begins by examining the metamaterial design's essential time and FD responses and then investigates how domain size, boundary conditions, and loading types affect wave propagation characteristics. Subsequently, the study compares the metamaterial performance against

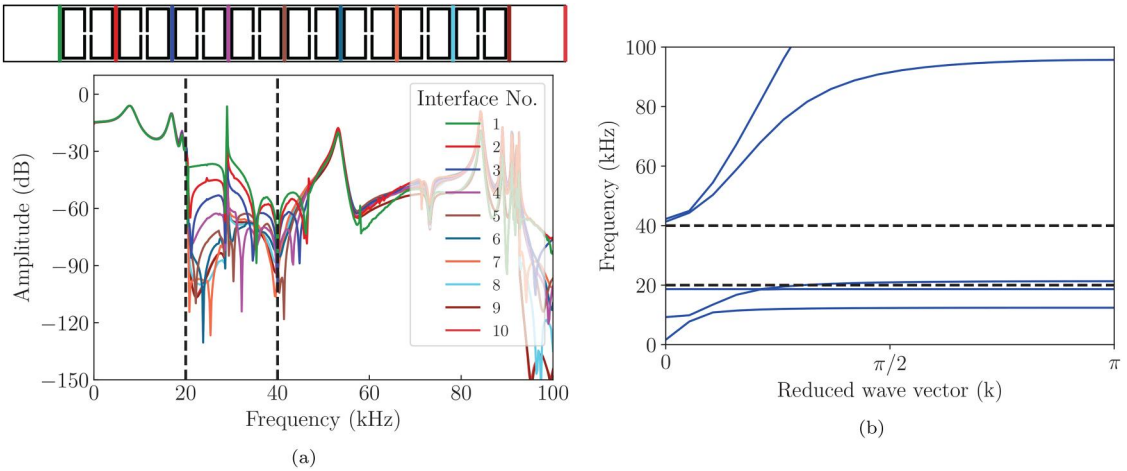

Figure 3. (a) FT of the energy transfer. The locations of the interfaces are highlighted above with the same colors (numbering is from left to right). Stopband of the MM is designed to be around 20–40 kHz, indicated with dashed lines. (b) Band structure of the unit cell.

conventional and alternative designs, explores graded configurations, and evaluates the impact of material damping. Through this progression, the investigation seeks to understand how these structures can be optimized for impact mitigation applications.

3.1. Size effect and transient response

3.1.1. TD and FD response of the MM

Before examining specific design parameters, this work first analyzes the fundamental response characteristics of the metamaterial slab in both time and frequency domains. This analysis provides baseline insights into how stress waves propagate through the structure and how the resonant elements engage with the incident wave.

The von-Mises stress fields plotted on the slab at different time values are illustrated in Figure 2. High-resolution visualization of the stress is accomplished by using very small elements. First, after the projectile impact, most of the stress wave reflects (denoted with R) from the first MM cell's free surface, while the rest travels through the outer walls. Then, the resonators of the MM array start to engage with the wave (denoted with E). Cell engagement speed is much lower than the wave speed of the material. This behavior reduces the effective energy transfer speed of the slab. The reduction in downstream cell engagement can be seen in later steps by comparing the overall von-Mises stress magnitude inside the resonators.

Next, the FD response is analyzed by plotting, at each interface, the Fourier transform (FT) of the energy flux density in Appendix Equation (14), evaluated using the average stress and the conjugate of the average velocity vectors, as shown in Figure 3a. This analysis focuses on the 0 to 100 kHz range. The FD bandgap for this design extends from 20 to 40 kHz. This plot shows that energy magnitude in all interfaces remains nearly identical below 20 kHz. Above this value, a consistent decrease in the magnitude of energy transfer at each progressive interface is observed. The magnitude levels get close to each other again after the upper bound. In addition, a peak occurs at 30 kHz, which represents truncation resonance and was recently explained in [54]. The band structure of the unit cell appears in Figure 3a.

The agreement between TD and FD methods confirms the consistency of the computational predictions regarding the existence of the low-frequency bandgap from 20 to 40 kHz. The band structure of the unit cell is shown in Figure 3b. Both TD and FD are linear-elastic numerical models, and the agreement between them should be interpreted as model-to-model consistency, rather than experimental validation. True validation would require comparison with experimental data or analytical solutions, which are beyond the scope of this paper. This cross-verification supports the reliability of the TD method for the following studies.

3.1.2. Domain size

To determine the optimal configuration for practical applications, this investigation examines how the number of metamaterial cells affects wave propagation and energy attenuation. This study compares four different slab lengths to understand the relationship between the array size and its performance. The analysis investigates the effect of the domain (slab) size on the wave propagation to select one size for further analysis.

The frequency signature of the wave changes after each unit cell, increasing the number of cells, which will affect the total energy attenuation in a manner not proportional to the slab length. The analysis examines four slabs with 4, 8, 16, and 32 resonant cells, given in Figure 4a insert, and loads them with a projectile of length $l_p = 20$ mm while keeping the back face traction-free. In this figure, the final resonant interface appears colored to represent the interfaces where the comparison takes place.

The energy transfer at each slab's final interface is represented in Figure 4a. The energy transfer requires different times to reach a plateau. This time correlates with the domain size. Regarding the absolute final magnitude of energy transfer, the 8-cell slab is more efficient at reducing the transmitted energy than the others. Since this domain

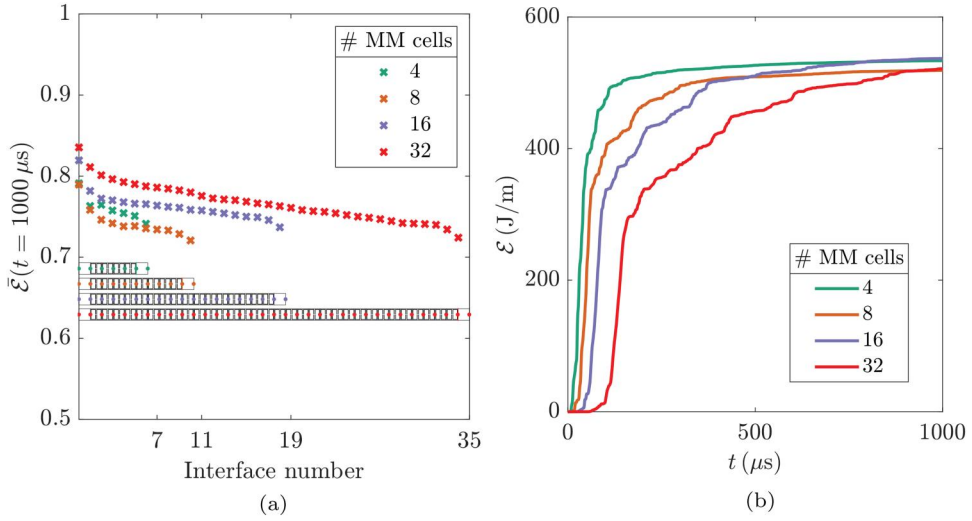

Figure 4. Domain size comparison. (a) Energy transfer magnitude at 1000 μs in between cell interfaces for 4, 8, 16, and 32 cell slabs, normalized by initial projectile energy. (b) Energy transfer plotted against time at the final resonant cell interface for 4, 8, 16, and 32 cell slabs.

size is small, the energy transfer is faster to reach the plateau. The difference between the terminal values of the 4 and 8 cells is around 3%. The reflections inside the domain cause the 4-cell slab to have a slightly higher terminal value than the 8-cell slab. Energy transfer in the 16-cell slab is higher than in the 8-cell slab after a time at the final interface, as reflected in the crossing in Figure 4a, due to the interaction between the length scale of the projectile and the total size of the slab.

To compare the performance throughout the domain, the energy transfers of all interfaces of each slab length are compared in Figure 4b at time 1000 μs. The energies are normalized by the initial projectile kinetic energy, represented by $\overline{\mathcal{E}}$. The projectile maintains a nonzero velocity after the impact, explaining the normalized energy transfer values of less than one, ranging from 0.78 to 0.83, for the first interfaces. The design that reduces energy transmission the most is 8 cells with 72% energy attenuation at the final interface relative to the initial kinetic energy of the projectile. Since the 8-cell slab performs better from the two perspectives above, this work restricts the subsequent studies to 8-cell slabs.

3.2. Effect of boundary conditions

3.2.1. Back face boundary conditions

The practical performance of metamaterial slabs depends significantly on their boundary conditions. This section examines how different back-face conditions, traction-free versus transmitting, influence wave propagation and energy transfer characteristics. The analysis examines these effects using stress and energy metrics to understand their practical implications.

Boundary conditions bring additional complexities to the performance of these slabs. First, the wave motion is directly affected by the frequency content of the loading, which is a function of the loading type and time scale. For example, the response of the MM to a projectile impact would be different from that of a blast loading. Second, the response of identical-length MM and comparison slabs will differ due to their different effective wave properties. The effect of the front face loading, i.e. PT, PV, PI, and blast, is discussed in Section 3.2.2. On the other hand, the back-face boundary condition affects the response through reflection and/or transmission at this boundary. It can be traction-free or rigid (fully reflecting), transmitting (non-reflecting), or partially reflective, depending on the impedance of the backing medium. In this section, the analysis compares traction-free and transmitting back-face boundary conditions as two extreme cases.

Initially, the back-face boundary is set to traction-free. The front face is loaded with the projectile impact. The simulation is run for 200 μs. A monolithic slab with the same physical length (10 cells) is simulated with the same conditions, and the results are compared with the MM. The average stress and energy transfer interface locations are given in Figures 5a and b, respectively. Quantities are plotted at the first, second, sixth, and tenth interfaces, corresponding to the impact interface, the first MM interface after the monolithic protective cell, the MM interface in the middle, and the final MM interface before the back monolithic cell.

The average stress results, illustrated in Figure 5a, demonstrate significant differences between MM and monolithic slabs. The monolithic slab has a much higher average stress magnitude throughout the slab, whereas MM has a broader frequency content and lower magnitude stress flux. An investigation into stress peaks unveils that the MM slab has five stress peaks at its initial interface and two within its internal domain. In contrast, the monolithic slab exhibits nine stress peaks at all its interfaces. This pattern of stress peaks remains consistent under various loading conditions, such as prescribed traction with a square stress pulse (not shown here). Furthermore, the analysis of stress dynamics at the impact interface for the MM configuration, denoted by the black curve in Figure 5a, showcases a complex contact relationship characterized by multiple peaks and drops during the initial phase of the simulation.

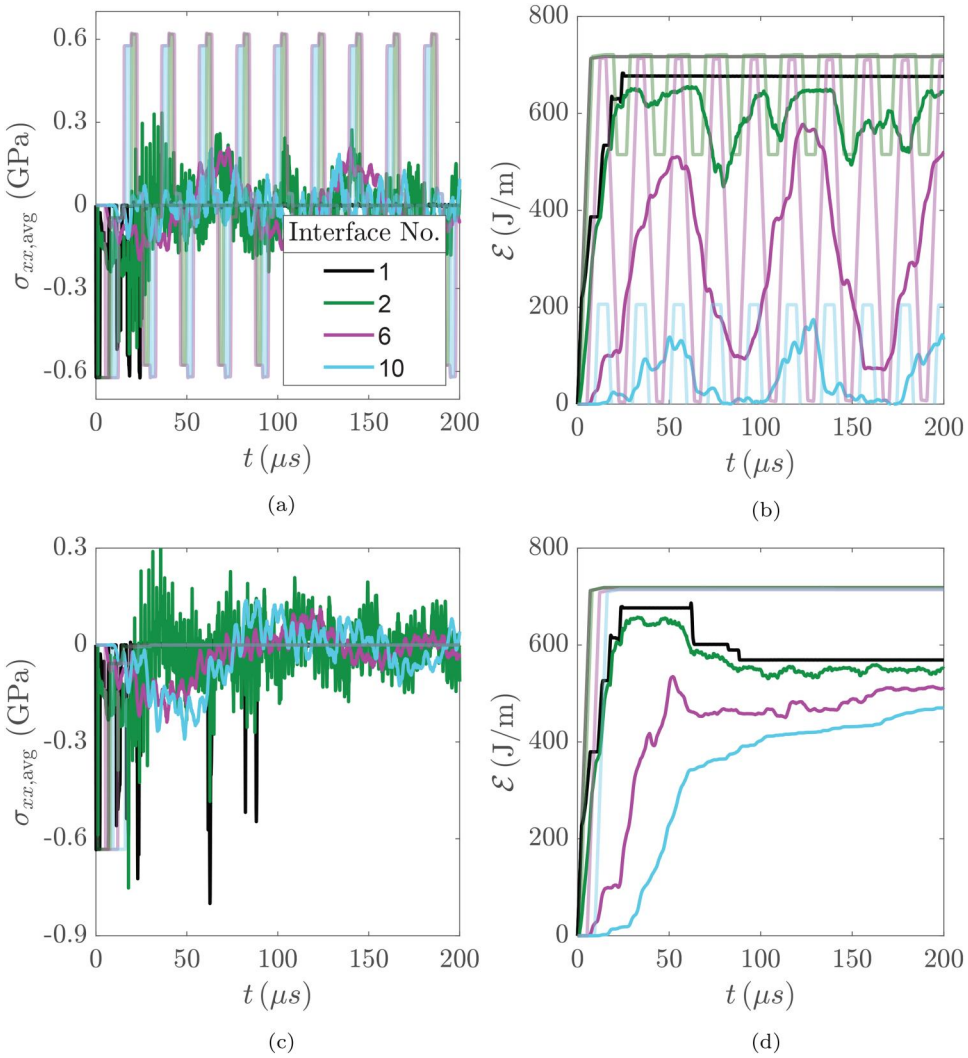

Figure 5. Comparison of (a, c) average stress and (b, d) energy transfer as functions of time at different interfaces for MM (solid) and monolithic (transparent) slabs with traction-free (top) and transmitting (bottom) boundary condition on the back-face under projectile impact.

Next, the examination of energy transfer from Figure 5b reveals several noteworthy observations. The peak energy transfer level at the terminal interface of the MM slab is approximately 15% lower than that of the monolithic slab. Furthermore, the time taken to reach half of the peak energy transfer value at the terminal interface for the MM configuration is approximately five times longer compared to the monolithic structure. This prolonged transmission time signifies the ability of the MM configuration to achieve a significant reduction in wave propagation speed. Additionally, a comparison between the upstream and downstream interfaces highlights the MM's capacity to diminish high-frequency content in the incoming wave. It must be noted that due to the limiting nature of the back face boundary conditions, these observations will be further evaluated for a more practical case.

Subsequently, referring to Figure 5 bottom row, the analysis explores the impact of transmitting back-face boundary conditions. The average stress results appear in Figure 5c. Comparison with Figure 5a reveals notable distinctions between the solutions corresponding to traction-free and transmitting back-face boundary conditions. In the monolithic slab, the results show no tensile stress, given the lack of wave reflection. Conversely, the domain in the MM configuration observes tensile stress, stemming from its inherent microstructural features. Specifically, the presence of free surfaces within the domain leads to the generation of tensile-release waves. It is crucial to note that this boundary condition represents an idealized scenario, as reflections would be expected in real-world applications. However, similarly to what was observed earlier, the number of stress peaks reduces to two from five under the transmitting boundary condition. Another notable observation is that the contact history between the projectile and the MM is noticeably prolonged in the case of the MM configuration when compared to the traction-free scenario.

The differences between the two slabs are further examined by referring to energy transfers in Figure 5d. Specifically, the magnitude of energy transfer within the monolithic domain experiences a rapid increase as the elastic wave propagates. In contrast, the MM exhibits a more gradual increase further into the domain. Decrements in the energy transfer correspond to energy flow through the impacted side. The extent of energy attenuation by the slab

can be quantified by comparing the energy transfers at the first and final interfaces. The MM attenuates approximately 30% of the incoming energy, while the monolithic completely transfers it. Furthermore, akin to our prior findings, the time required to reach the plateau is significantly extended for the MM configuration. These outcomes underscore the potential practical utility of the MM.

Given the alignment of main conclusions from the two back-face boundary conditions, *i.e.* slow down of the wave and decay of energy transfer for the MM design, this study uses a transmitting back-face boundary condition for the remainder of this paper. This approach eliminates the influence of reflections and facilitates the characterization of energy attenuation as the energy curves can reach a plateau.

3.2.2. Front face boundary conditions

The frequency-dependent nature of the MM causes different energy attenuation efficacies under different loading scenarios. To examine the attenuation performance, the back face is set to a transmitting boundary condition, and four different types of loading given in Section 2 are applied with the same time scale and stress magnitude at the front face. Figure 6 illustrates the ratio of the energy transfer of the last and first interfaces at 200 μs for different types of loading. In the figure, a single bar equal to one represents the ratio for the monolithic slab for all loading types since no wave attenuation mechanisms exist. For the MM slab, blast and projectile impact loading types significantly have lower energy transfer ratios, around 48% and 68%, while ratios for PT and PV ratios are higher at 71% and 82%, respectively. The difference in the energy transfer can be attributed to the frequency content of the loading. Moreover, the energy transfer ratio for the projectile impact increases with the projectile length. For instance, the energy transfer ratio for a 2.5 mm projectile impact results in 22% transferred energy. The results demonstrate that, unsurprisingly, the energy attenuation is more favorable when the incident frequency content is concentrated around the bandgap frequency.

In conclusion, the MM outperforms the monolithic slab under all loading conditions except for PT, in which it experiences a higher absolute energy transfer at the first interface. However, the energy transfer decay is substantial for all loading conditions, and generally, the downstream interfaces show lower absolute energy transfer. Moreover, the wave slows down substantially in all cases. In the next section, the comparison expands further, considering other types of non-resonant unit cells.

3.3. Comparison with non-resonant microstructures and heuristic optimization

3.3.1. Comparison slabs

This study compares the stress and energy metrics of H-cell arrays with the monolithic, equal gap, and square gap cells given in Figure 1. This comparison helps isolate the specific benefits of the resonant architecture versus other potential microstructures. The analysis conducts comparisons with the

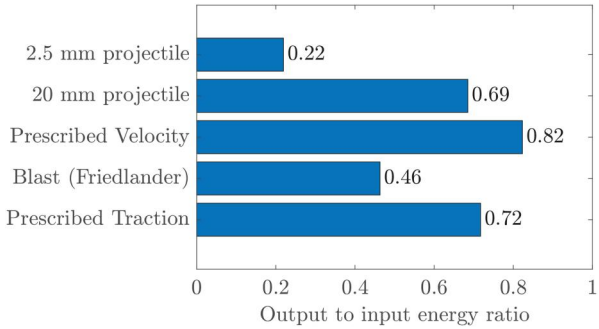

Figure 6. Energy transfer magnitude ratios at the penultimate and incident interfaces.

30 m/s, 20 mm projectile and transmitting back-face boundary, as explained in the previous sections. All slabs have 8 unit cells (or the same thickness in the case of the monolithic slab), excluding protective monolithic cells on both ends.

The average stress and energy transfer results obtained from the comparison of these unit cells are plotted in Figures 7a and b, respectively. The average stress plot depicts the substantial decrease in the maximum stress magnitude of the MM when compared with the other slabs. The other microstructured slabs also create tensile release waves, similar to the MM. Even though the other comparison cells indicate wave slowdown, the results show that the MM performs best in that metric. Furthermore, the energy transfer is significantly lower than that of the other slabs. The final energy transfer value is around 33% lower for the MM than for the monolithic design. In comparison, the energy reduction for the next best design (equal gap) is only around 18%. These observations underline the importance of the resonant microstructure compared to simple cellular ones for the mitigation of stress waves.

3.3.2. Heuristic designs

In this section, possible nonuniform (graded) MM arrays are explored to improve the impact response of the structure further. A 16-cell MM slab has been modified by changing the material properties after every four cells, thus resulting in a four-by-four structure shown in Figure 8b. In practice, it is far more feasible to create such a gradation through geometric modifications. However, for the sake of computational consistency and speed, the concept is tried here using density and modulus modifications. To study directionality considerations, the same slab has been flipped and analyzed, as shown in Figure 8c. To showcase the performance difference, the initial four-cell group (A) has kept the same properties as alumina, and the following groups' densities and Young's moduli are modified to have bandgaps centered around two times lower bandgap frequencies progressively:

$$\rho_A = \frac{\rho_B}{2} = \frac{\rho_C}{4} = \frac{\rho_D}{8}, \tag{1}$$

$$E_A = 2E_B = 4E_C = 8E_D. \tag{2}$$

Consequently, the wave speed is also modified and decreased by a factor of 2 each time from A to B to C to D.

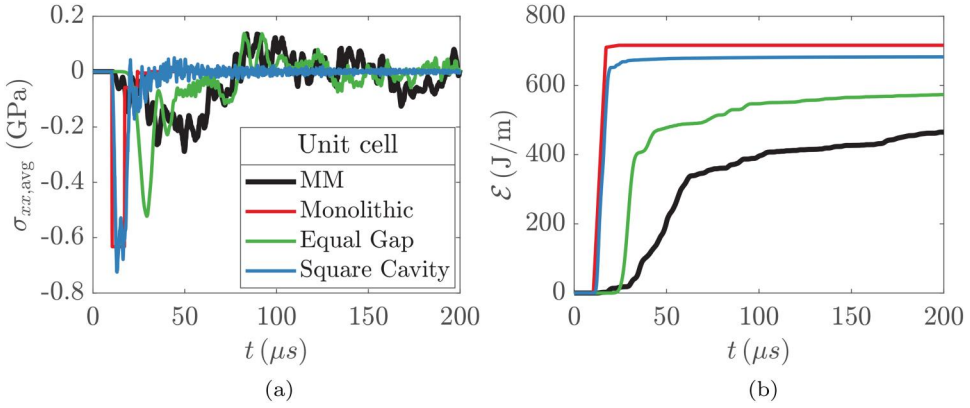

Figure 7. Comparison of (a) average stress and (b) energy transfer as functions of time at the final interface for MM and comparison slabs with transmitting boundary condition on the back-face under projectile impact.

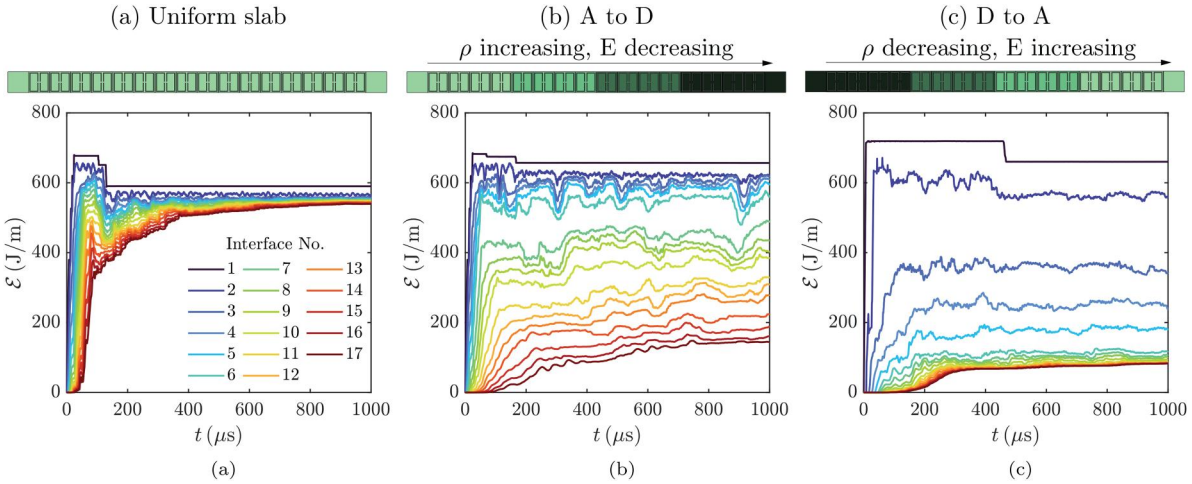

Figure 8. Energy transfer comparison for the uniform and graded designs: (a) uniform slab, (b) A-to-D corresponding to increasing ρ and decreasing E toward the back face, and (c) D-to-A.

On the other hand, the impedances are equal to those of the original material, that is, for cells A. For a unit-cell that behaves like a simple mass-spring resonator, which is a first-order model for sub-wavelength locally resonant MM, the resonance that opens the bandgap is set by [55]:

$$f_r = \frac{1}{2\pi}\sqrt{\frac{k}{m}} \approx \frac{1}{2\pi}\sqrt{\frac{cE}{\rho V}}, \tag{3}$$

where f_r, c, and V are the intrinsic resonance, the wave speed, and the volume, respectively. $k \propto E$ is the effective stiffness and $m \propto \rho$ is the resonator mass (geometry held fixed, so c/V is constant). Hence, the bandgap's center frequency scales with the square root of the modulus-to-density ratio, $f_r \propto \sqrt{E/\rho}$.

Replacing alumina (material A) with materials B, C, or D whose moduli and densities satisfy Equations (1) and (2) multiplies the center frequency by the factor:

$$\lambda = \sqrt{\frac{E/E_A}{\rho/\rho_A}} \quad \Rightarrow \quad f_r^{\mathrm{new}} = \lambda\, f_r^A. \tag{4}$$

The resulting shifts, keeping the original 20 to 40 kHz gap of alumina (material A) as a reference, are listed in Table 2.

The energy transfer plots for uniform material, A-to-D, and D-to-A graded slabs are given in Figures 8a–c, respectively. The superior performance of graded configurations stems from fundamental wave-metamaterial interaction mechanisms. In uniform arrays, energy "capture" capacity quickly stagnates because all cells share identical resonance characteristics, leading to spectral filtering that progressively mismatches downstream cells with the modified wave content. Graded designs overcome this limitation through systematic variation of local resonance frequencies that maintain optimal wave-cell interaction throughout the structure.

The A-to-D configuration (decreasing stiffness and increasing density toward the back face) creates a cascade of successively lower resonance frequencies that sequentially engage with the wave as its spectral content shifts. This sequential resonance mechanism enables broadband energy capture, where each cell group optimally attenuates different frequency components of the incoming wave. The impedance-matched design (constant acoustic impedance across materials) ensures efficient energy transfer between cell groups, while the varying wave speeds create additional wave interaction time scales that enhance overall attenuation. Conversely, the D-to-A configuration concentrates most attenuation in the first group, demonstrating the

Table 2. Scaling of the bandgap center frequency when substituting material A (alumina) by materials B–D.

Material	E/E_A	ρ/ρ_A	$\lambda = \sqrt{(E/E_A)/(\rho/\rho_A)}$	New bandgap (kHz)
A (baseline)	1	1	1	20–40
B	1/2	2	1/2	10–20
C	1/4	4	1/4	5–10
D	1/8	8	1/8	2.5–5

critical importance of resonance frequency ordering in graded designs.

The effect of the difference in wave speed of the materials can be clearly seen in the wave arrival time at the final interface. When the heavier and slower cell is in the front, the energy transfer magnitude is lower, and the wave arrival time is longer. The terminal energy magnitude of the D-to-A slab is 6.5 times lower than that of the uniform slab. Relative to the 8-cell uniform MM slab, the A-to-D and D-to-A graded slabs reduce transmitted energy at the penultimate interface by 3.6 and 6.3 times, respectively. In other words, the A-to-D and D-to-A graded slabs provide 72% and 84% improvements over the base case uniform slab, respectively. These are particularly encouraging results that show the impact of graded MM design. Further investigation is needed to better understand the possible geometric designs that can achieve this performance.

3.4. Effect of material damping

Material damping is a critical mechanism for energy attenuation. Especially for MMs, damping can be used as an advantageous mechanism to reduce energy transfer further. For this reason, material damping is added to the linear finite element model of the MM and monolithic slabs, and the behavior is explored for different damping constants. Material damping in finite element modeling can be treated with mass-proportional or stiffness-proportional damping. LS-DYNA calculates internal forces by integrating stresses over the element area. Damping forces are added to these forces by [56],

$$\mathbf{a}^n = \mathbf{M}^{-1}\left(\mathbf{P}^n - \mathbf{F}^n - \mathbf{F}^n_{\text{damp}}\right), \tag{5}$$

where $\mathbf{a}^n$ is the acceleration vector, $\mathbf{M}$ is the mass matrix, $\mathbf{P}^n$ and $\mathbf{F}^n$ are the external and internal load vectors, respectively, and $\mathbf{F}^n_{\text{damp}}$ is the damping force, calculated by [57],

$$\mathbf{F}_{\text{damp}} = \sum D_s m\mathbf{v} = \sum 4\pi f \zeta m\mathbf{v}, \tag{6}$$

where D_s is the damping constant, m is the node's mass, $\mathbf{v}$ is the node's velocity vector, ζ is the nondimensional modal damping ratio, and f is the damping frequency. The summation $\sum$ refers to the assembly of nodal forces to $\mathbf{F}_{\text{damp}}$. Another constant that describes damping is the quality factor or internal friction, $Q^{-1} = 2\zeta$ [58]. Deduced from the reported Q^{-1} in [59], the critical damping ratio for alumina at room temperature is $\zeta = 2.5 \times 10^{-5}$.

Next, we relate the damping force to the Rayleigh damping. Damping can be modeled using classical Rayleigh damping, where the damping matrix, $\mathbf{C}$, is calculated by a linear combination of mass and stiffness matrices, $\mathbf{M}$ and $\mathbf{K}$, respectively [56,60],

$$\mathbf{C} = \alpha\mathbf{M} + \beta\mathbf{K}, \tag{7}$$

where α and β are the Rayleigh damping coefficients. The contribution from the α term is equivalent to the damping force in D_s. More specifically, $\alpha = 2\pi f\zeta$, where f is the frequency for which the value of the nondimensional modal damping ratio ζ is measured. This corresponds to $f \approx 10$ kHz in [59], resulting in a baseline α of around 1.6/s. As for an upper bound for α, the critical damping ratio for alumina with a void ratio of 2% can go up to $\zeta = 0.01$ [61]. This is a realistic upper bound to consider for 3D-printed ceramics, since, depending on the printing parameters, such void ratios can be observed. The corresponding α to this upper bound ζ is around 600/s. Because the actual damping parameter of the ceramic is ambiguous, the subsequent analysis uses α values ranging from around 10^{-2} to 10^6/s. This not only contains the range of values reported based on the results in [59] and [61] but also can examine how the response is affected by lower and higher damping values.

To test robustness, we repeat the MM and monolithic comparison under pure stiffness-proportional Rayleigh damping. We choose β so that the modal values match the $\zeta(\omega)$ achieved by the α values provided above. For a mode with circular frequency $\omega = 2\pi f$, classical Rayleigh damping gives the nondimensional modal damping ratio and the modal energy decay rate as [62],

$$\zeta(\omega) = \frac{\alpha}{2\omega} + \frac{\beta\omega}{2}, \tag{8}$$

$$\dot{E}(\omega, t) = -2\zeta(\omega)\omega E(\omega, t) = -\left(\alpha + \beta\ \omega^2\right)E(\omega, t), \tag{9}$$

where α (1/s) and β (s) are the mass- and stiffness-proportional coefficients shown in Equation (7), $E(\omega, t)$ is the modal energy, and $\dot{E}$ is its time derivative, or the modal energy decay rate. To compare α-only and β-only cases with equal dissipation, we match the per-mode damping at a reference circular frequency $\omega_{\text{ref}} = 62\,831$ rad/s from [59],

$$\zeta_\alpha(\omega_{\text{ref}}) = \zeta_\beta(\omega_{\text{ref}}) \iff \frac{\alpha}{2\omega_{\text{ref}}} = \frac{\beta\omega_{\text{ref}}}{2} \Rightarrow \beta = \frac{\alpha}{\omega^2_{\text{ref}}}. \tag{10}$$

In this work, the classical Rayleigh damping, $C = \alpha\mathbf{M} + \beta\mathbf{K}$, is strictly used as a computational surrogate for small-strain dissipation. Neither the $\alpha\mathbf{M}$ nor the $\beta\mathbf{K}$ is a physics-based constitutive law for additively manufactured alumina[1]. In Equation (8), $\alpha\mathbf{M}$ implies unrealistically large damping as $\omega \to 0$ and $\beta\mathbf{K}$ implies unbounded damping as $\omega \to \infty$. Real ceramics exhibit mechanisms such as microcrack friction/closure, grain-boundary sliding, pore-interface slip, and microplasticity; these are frequency-, amplitude-, temperature-, and history-dependent, generally non-

[1]However, they are widely used in TD analysis because of their relative ease of implementation (e.g., no convolution operator is required).

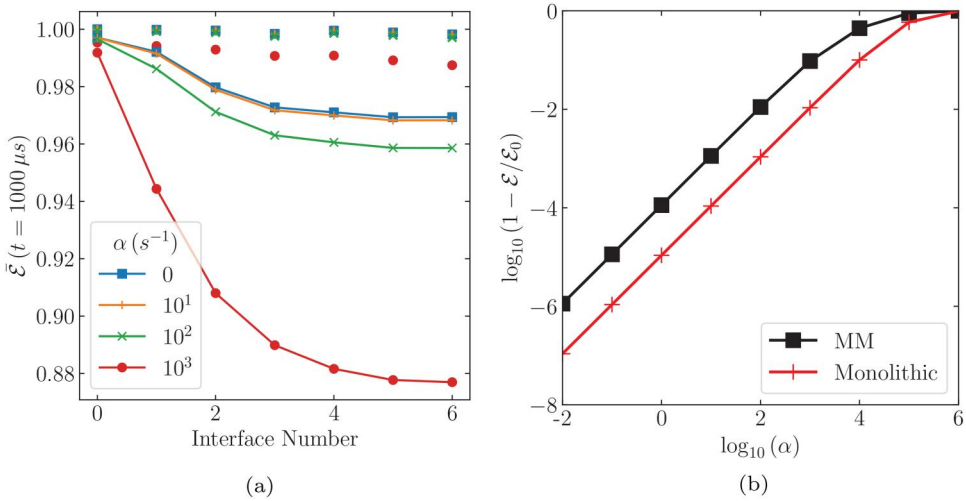

Figure 9. (a) Normalized energy transfer comparison for different damping constant values for $\alpha\mathbf{M}$. values for MM are shown with lines and markers, whereas monolithic is shown with markers only. (b) Normalized difference of damped and lossless energy transfers plotted against the damping constant α (s^{-1}) for the MM and monolithic slabs. Markers represent the values used in the simulations.

proportional, and are better represented by complex moduli (e.g. nearly constant loss factors over bands [63]), hysteretic models, or explicit damage/fracture laws. Consequently, calibrating (α, β) at one or two anchor frequencies can mimic target modal loss locally, but predictions outside those bands lack physical fidelity. Thus, $\alpha\mathbf{M}$ and $\beta\mathbf{K}$ are employed only to investigate whether trends persist under different loss models. The magnitude attenuations obtained should be treated as preliminary, and the actual material loss should be calibrated by experiments. We refer the reader to [63] and [64] for a more detailed comparison of various loss models. We will next discuss the effect of the two damping models on the performance of MM and monolithic slabs.

Figure 9a compares energy transfer at different interfaces for varying α and for MM and monolithic designs. The energy transfer values are normalized with respect to the energy of the first interface of the lossless case, similar to the analysis in Section 3.2.2. What stands out in this figure is the vast disparity between the energy transfer difference at the final interface for the same damping constant, *i.e.* $\alpha = 10^2/\text{s}$. The energy transfer difference with the lossless system becomes significant for damping constants higher than $10^2/\text{s}$. Even though the reported damping constant of alumina from [59] is smaller than this value, as discussed above, larger α can be encountered for higher void ceramics [61]. Likewise, changing to a different material with a higher damping constant may also take advantage of lower stress magnitude and energy transfer.

To compare the effect of different damping coefficients for the MM and monolithic slabs, the energy transfer at the final interface for the damped slabs ($\mathcal{E}$) is subtracted from the lossless system ($\mathcal{E}_0$) and normalized with respect to $\mathcal{E}_0$. A value close to zero ($\log(1 - \mathcal{E}/\mathcal{E}_0) \to -\infty$) means that the lossy system provides no advantage in further energy decay relative to the lossless one, while as this ratio tends to one ($\log(1 - \mathcal{E}/\mathcal{E}_0) \to 0$). The damping has a significant effect and reduces the relative energy transfer to zero. Figure 9b plots the normalized energy ratio of both slab designs against α. The slopes of the log-log curves are equal to one. A one-dimensional analysis, not presented here for brevity, confirms this slope for the monolithic design. The energy transfers in both cases are getting closer to zero for high damping constants. For the lower damping constants, there is a constant difference between the MM and monolithic that can be attributed to the higher structural damping capacity of the MM. That is, there is even an added benefit relative to a monolithic material response in terms of the energy decay of the MM design when material damping is considered. This higher potential can be exploited for energy mitigation applications such as impact and blast protection.

With the matched β targets using Equation (10), trends in transmitted energy at the penultimate interface remain qualitatively unchanged for the middle damping range. Because the metamaterial shifts spectral energy toward lower ω (resonant trapping/dispersion), β-loss is intrinsically less effective at very low ω than α-loss, explaining the observed convergence of MM and monolithic for $\beta \to 0$; at intermediate and higher ω the trends re-separate. Full curves and parameters are provided in Supplement SM-1. Large β values imply smaller time steps, necessitating an implicit time-integration scheme. To meet this requirement, the analysis uses 4-cell slabs (with protective monolithic cells at both ends, as explained in Section 3.1.2) and a prescribed traction loading condition.

4. Summary and conclusions

This linear TD study demonstrates that the proposed locally resonant architecture slows and redistributes stress waves and, within the mass-proportional Rayleigh damping model, amplifies dissipation relative to monolithic and non-resonant microstructures. These are pre-failure mechanisms: they act before nonlinear damage initiates. As such, the conclusions should be interpreted as architectural potential for managing waves rather than as established protective performance under severe impact. The essential next step is a nonlinear study (progressive damage, rate effects, contact in cavities) and experiments on printed alumina to validate the

protective value. We therefore position grading and resonance-based slowdown as strategies that could delay damage initiation, pending nonlinear/external validation. The key findings from this systematic investigation include:

1. **Effect of domain size:** The number of cells in the MM slab reaches optimal performance only after (in this case) eight cells. Beyond this threshold, changes in the frequency content of the propagating wave inhibit further energy transfer reduction due to the narrow bandwidth limitations of uniform cell designs. The performance saturation occurs because downstream cells encounter waves with modified spectral content that no longer align optimally with their resonance characteristics.
2. **Loading type dependency:** The nature of the loading affects the response drastically due to the frequency-dependent characteristics of metamaterial bandgaps. Shorter projectile impacts generate broader frequency content that better excites the resonant elements, resulting in enhanced energy attenuation (22% energy transfer for 2.5 mm projectiles versus 68% for 20 mm projectiles). Blast and projectile loading achieve superior performance (48% and 68% energy transfer ratios) compared to prescribed traction and velocity conditions (71% and 82%) due to frequency content alignment with the metamaterial.
3. **Comparison with alternative designs:** The resonant metamaterial architecture demonstrates superior performance compared to monolithic and other microstructured designs through unique wave attenuation mechanisms. The H-cell resonator creates internal degrees of freedom that engage with incident waves through local resonance, fundamentally different from simple geometric effects in non-resonant microstructures. Peak energy transfer at the final interface reaches up to 78% and 60% lower than monolithic and equal gap designs, respectively. The metamaterial achieves a five-fold increase in wave arrival time while reducing stress peak multiplicity.
4. **Graded design mechanisms:** Graded designs overcome the performance saturation through systematic variation of local resonance frequencies that maintain optimal wave-cell interaction throughout the structure. These configurations create a cascade of successively lower resonance frequencies that sequentially engage with the wave as its spectral content shifts, enabling broadband energy capture where each cell group optimally attenuates different frequency components. Graded designs can provide up to 84% improvement in lowering the energy transfer over the uniform design.
5. **Material damping amplification:** Metamaterial structures exhibit multiplicative enhancement of material damping effects compared to conventional designs when using the mass-proportional Rayleigh damping model. The resonant microstructure amplifies energy dissipation mechanisms, achieving up to four times better performance than monolithic slabs for equivalent damping coefficients. This amplification occurs because the resonant elements create internal wave motion that increases the effective path length and interaction time for dissipative mechanisms.

Further research should investigate the nonlinear response of the structure. Material damping and failure account for energy dissipation while drastically changing the stress wave profile. Preliminary results, accounting for material failure (to be presented in an upcoming publication), indicate that the MM slab significantly improves the energy transfer attenuation compared to the monolithic slab, even in the presence of widespread failure. Planned nonlinear studies include progressive damage modeling with rate-dependent material behavior under high-velocity impact, and contact dynamics within resonator cavities during extreme loading. Experimental validation through ballistic testing of additively manufactured ceramic specimens will complement computational findings, focusing on energy dissipation measurements, failure pattern characterization, and validation of graded design performance under controlled impact conditions. Further analysis focusing on 2D wave propagation in MM structures has also underlined the potential to leverage anisotropic wave speed with designs developed using generative neural networks to improve impact mitigation further using microstructured media [65].

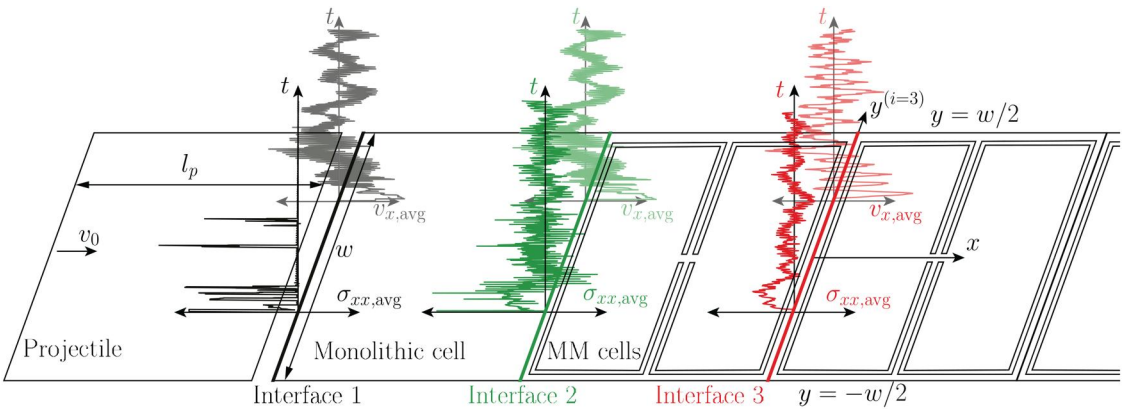

Figure 10. Schematic representation of interfaces at the slab with average stress and velocity values plotted against time. Metamaterial slabs have protective monolithic cells on both ends.

Acknowledgements

The authors wish to thank DEVCOM Army Research Laboratory for continued support throughout this effort. This research was supported by DEVCOM Army Research Laboratory through Cooperative Agreement W911NF–20–2–0147, with additional support from The University of Tennessee. The authors would also like to thank the University of Tennessee Infrastructure for Scientific Applications and Advanced Computing (ISAAC). A portion of the computation for this work was performed with ISAAC computational resources.

Author contributions

CRediT: **Erdem Caliskan**: Data curation, Formal analysis, Investigation, Methodology, Software, Validation, Visualization, Writing – original draft; **Willoughby Cheney**: Software, Validation, Visualization; **Weidi Wang**: Formal analysis, Methodology, Validation, Writing – review & editing; **Thomas Plaisted**: Conceptualization, Formal analysis, Methodology, Writing – review & editing; **Alireza V. Amirkhizi**: Conceptualization, Formal analysis, Funding acquisition, Methodology, Project administration, Writing – review & editing; **Reza Abedi**: Conceptualization, Formal analysis, Funding acquisition, Methodology, Project administration, Supervision, Writing – review & editing.

Disclosure statement

No potential competing interest was reported by the authors.

Appendix A: Computation of interface TD and FD quantities

Quantitative comparisons are conducted by spatial averaging of the quantities of interest over the interface areas between unit cells (and the same locations for the monolithic slab), and tracking the temporal evolutions of these average quantities. Interfaces numbering, along with example average stress and velocity quantities, are illustrated in Figure 10. Here, the average stress and velocity values are plotted in two different time axes for the first three interfaces. l_p and v_0 are the projectile length and initial speed, respectively, while w is the width, which is fixed to 10 mm. Traction at a node as a function of y-coordinate and the time, t is calculated by,

$$\mathbf{T}^{(\mathbf{n})}(y,t) = \boldsymbol{\sigma}(y,t)\cdot\mathbf{n}, \tag{11}$$

where $\boldsymbol{\sigma}$ is stress interpolated at the nodes and $\mathbf{n}$ is the normal vector. Then, the energy flux density per unit time and spatial area, *i.e.* power, ($\mathcal{P}$) and the energy transfer ($\mathcal{E}$) at the interface are calculated as:

$$\mathcal{P}(y,t) = \mathbf{T}^{(\mathbf{n})}(y,t)\cdot\mathbf{v}(y,t), \tag{12}$$

$$\mathcal{E}(t) = \int_0^t\int_{-w/2}^{w/2}\mathcal{P}(y,t)\mathrm{d}y\,\mathrm{d}t. \tag{13}$$

The results are plotted as stress and energy at the interfaces between unit cells. Two metrics have been used to evaluate the performance: energy mitigation and slowdown of waves. The *energy transfer ratio* is obtained using the ratio of the energy transfer of the last interface to that of the first one. The *half-time* quantifies the time it takes for the energy transfer to reach half of its peak value at each measurement location and is used to measure wave slowdown. These values have been used to compare the MM slab with the monolithic and the other comparison slabs.

TD results are turned into FD by applying the Fourier transform (FT) to the spatial averages of stress and velocity. The FT of energy flux density $\mathcal{P}$ is obtained from the Poynting relation as:

$$\hat{\mathcal{P}}(y,\omega) = 0.5\mathrm{Re}\left[\widehat{\mathbf{T}^{(\mathbf{n})}}(y,\omega)\cdot\hat{\mathbf{v}}^*(y,\omega)\right], \tag{14}$$

where $\hat{f}$ and z^* stand for the Fourier transform of function f and complex conjugate of number z, respectively, and Re is the real operator. The angular frequency is denoted by ω. We apply the Poynting relation to the average traction and the conjugate of the average velocity vectors to analyze the frequency content of the energy transfer.

References

[1] A. Srivastava, and J.R. Willis, Evanescent wave boundary layers in metamaterials and sidestepping them through a variational approach, Proc. Math. Phys. Eng. Sci., vol. 473, no. 2200, pp. 20160765, 2017. DOI: 10.1098/rspa.2016.0765.

[2] K.T. Tan, H.-H. Huang, and C.-T. Sun, Blast-wave impact mitigation using negative effective mass density concept of elastic metamaterials, Int. J. Impact Eng., vol. 64, pp. 20–29, 2014. DOI: 10.1016/j.ijimpeng.2013.09.003.

[3] E. Kim, J. Yang, H. Hwang, and C.W. Shul, Impact and blast mitigation using locally resonant woodpile metamaterials, Int. J. Impact Eng., vol. 101, pp. 24–31, 2017. DOI: 10.1016/j.ijimpeng.2016.09.006.

[4] A. Karakoti, S. Pandey, and V.R. Kar, Nonlinear transient analysis of porous functionally graded material plates under blast loading, Mater. Today: Proc., vol. 46, pp. 8111–8113, 2021. DOI: 10.1016/j.matpr.2021.03.051.

[5] C. Ding, L. Hao, and X. Zhao, Two-dimensional acoustic metamaterial with negative modulus, J. Appl. Phys., vol. 108, no. 7, pp. 074911, 2010. DOI: 10.1063/1.3493155.

[6] J. Jung, H.-G. Kim, S. Goo, K.-J. Chang, and S. Wang, Realisation of a locally resonant metamaterial on the automobile panel structure to reduce noise radiation, Mech. Syst. Sig. Process., vol. 122, pp. 206–231, 2019. DOI: 10.1016/j.ymssp.2018.11.050.

[7] V. Gorshkov, P. Sareh, N. Navadeh, V. Tereshchuk, and A.S. Fallah, Multi-resonator metamaterials as multi-band metastructures, Mater. Des., vol. 202, pp. 109522, 2021. DOI: 10.1016/j.matdes.2021.109522.

[8] S. Brûlé, E. Javelaud, S. Enoch, and S. Guenneau, Experiments on seismic metamaterials: molding surface waves, Phys. Rev. Lett., vol. 112, no. 13, pp. 133901, 2014. DOI: 10.1103/PhysRevLett.112.133901.

[9] L. Wu, and Z. Shi, Surface wave manipulation by metasurfaces in unsaturated soil: theoretical study, Int. J. Mech. Sci., vol. 286, pp. 109857, 2025. DOI: 10.1016/j.ijmecsci.2024.109857.

[10] J. Lv, M. Zhou, Q. Gu, X. Jiang, Y. Ying, and G. Si, Metamaterial lensing devices, Molecules, vol. 24, no. 13, pp. 2460, 2019. DOI: 10.3390/molecules24132460.

[11] P. Sheng, J. Mei, Z. Liu, and W. Wen, Dynamic mass density and acoustic metamaterials, Physica B., vol. 394, no. 2, pp. 256–261, 2007. DOI: 10.1016/j.physb.2006.12.046.

[12] H. Huang, and C. Sun, Wave attenuation mechanism in an acoustic metamaterial with negative effective mass density, New J. Phys., vol. 11, no. 1, pp. 13003, 2009. DOI: 10.1088/1367-2630/11/1/013003.

[13] C. Chu, A. Leichner, F. Wenz, and H. Andrä, Exploring vae-driven implicit parametric unit cells for multiscale topology optimization, Mater. Des., vol. 244, pp. 113087, 2024. DOI: 10.1016/j.matdes.2024.113087.

[14] S. Dalela, P. Balaji, and D. Jena, A review on application of mechanical metamaterials for vibration control, Mech. Adv. Mater. Struct., vol. 29, no. 22, pp. 3237–3262, 2022. DOI: 10.1080/15376494.2021.1892244.

[15] M. Mohsenizadeh, F. Gasbarri, M. Munther, A. Beheshti, and K. Davami, Additively-manufactured lightweight metamaterials for energy absorption, Mater. Des., vol. 139, pp. 521–530, 2018. DOI: 10.1016/j.matdes.2017.11.037.

[16] M.Y. Khalid, Z.U. Arif, A. Tariq, M. Hossain, R. Umer, and M. Bodaghi, 3d printing of active mechanical metamaterials: a

critical review, Mater. Des., vol. 246, pp. 113305, 2024. DOI: 10.1016/j.matdes.2024.113305.
[17] J. Han, X. Zhai, L. Wang, D. Zhang, J. Ding, W.W.S. Ma, X. Song, W.-H. Liao, L. Liu, J. Wu, and X.-M. Fu, Inverse-designed 3d sequential metamaterials achieving extreme stiffness, Mater. Des., vol. 247, pp. 113350, 2024. DOI: 10.1016/j.matdes.2024.113350.
[18] X. Wang, C. Zhang, S. Rui, C. Wu, W. Zhang, and F. Ma, Multi-scale material/structure integrated elastic metamaterial for broadband vibration absorbing, Mater. Des., vol. 238, pp. 112705, 2024. DOI: 10.1016/j.matdes.2024.112705.
[19] S. Huang, Z. Ma, and F. Wang, A multi-objective design optimization strategy for vertical ground heat exchangers, Energy Build., vol. 87, pp. 233–242, 2015. DOI: 10.1016/j.enbuild.2014.11.024.
[20] T. Fisher, Z. Kazancı, and J.H.S. Almeida, Jr, High-velocity impact response of 3d-printed composite mechanical metamaterials, Int. J. Mech. Sci., vol. 286, pp. 109905, 2025. DOI: 10.1016/j.ijmecsci.2024.109905.
[21] L. Brillouin, Wave *propagation in periodic structures: electric filters and crystal lattices*. McGraw-Hill Book Company, Incorporated, 1946.
[22] L. Liu, and M.I. Hussein, Wave motion in periodic flexural beams and characterization of the transition between Bragg scattering and local resonance, J. Appl. Mech., vol. 79, no. 1, pp. 11003, 2012. DOI: 10.1115/1.4004592.
[23] M.I. Hussein, G.M. Hulbert, and R.A. Scott, Dispersive elastodynamics of 1d banded materials and structures: analysis, J. Sound Vib., vol. 289, no. 4–5, pp. 779–806, 2006. DOI: 10.1016/j.jsv.2005.02.030.
[24] M.I. Hussein, M.J. Leamy, and M. Ruzzene, Dynamics of phononic materials and structures: historical origins, recent progress, and future outlook, Appl. Mech. Rev., vol. 66, no. 4, pp. 40802, 2014. DOI: 10.1115/1.4027795.
[25] Z. Liu, C.T. Chan, and P. Sheng, Three-component elastic wave band-gap material, Phys. Rev. B., vol. 65, no. 16, pp. 165116, 2002. DOI: 10.1103/physrevb.65.165116.
[26] M. Hirsekorn, Small-size sonic crystals with strong attenuation bands in the audible frequency range, Appl. Phys. Lett., vol. 84, no. 17, pp. 3364–3366, 2004. DOI: 10.1063/1.1723688.
[27] G. Wang, D. Yu, J. Wen, Y. Liu, and X. Wen, One-dimensional phononic crystals with locally resonant structures, Phys. Lett. A., vol. 327, no. 5–6, pp. 512–521, 2004. DOI: 10.1016/j.physleta.2004.05.047.
[28] Z. Liu, X. Zhang, Y. Mao, Y.Y. Zhu, Z. Yang, C.T. Chan, and P. Sheng, Locally resonant sonic materials, Science, vol. 289, no. 5485, pp. 1734–1736, 2000. DOI: 10.1126/science.289.5485.1734.
[29] R. Zhang, W. Ding, B. Fang, P. Feng, K. Wang, T. Chen, and J. Zhu, Syndiotactic chiral metastructure with local resonance for low-frequency vibration isolation, Int. J. Mech. Sci., vol. 281, pp. 109564, 2024. DOI: 10.1016/j.ijmecsci.2024.109564.
[30] S.A. Cummer, and D. Schurig, One path to acoustic cloaking, New J. Phys., vol. 9, no. 3, pp. 45–45, 2007. DOI: 10.1088/1367-2630/9/3/045.
[31] S. Zhang, J. Lou, H. Fan, and J. Du, A nonlinear acoustic metamaterial beam with tunable flexural wave band gaps, Eng. Struct., vol. 276, pp. 115379, 2023. DOI: 10.1016/j.engstruct.2022.115379.
[32] J. Lou, H. Fan, A. Zhang, M. Xu, and J. Du, A graded acoustic metamaterial rod enabling ultra-broadband vibration attenuation and rainbow reflection, Thin. Walled Struct., vol. 198, pp. 111716, 2024. DOI: 10.1016/j.tws.2024.111716.
[33] J. Lou, S. Zhang, H. Fan, X. Fang, and J. Du, Ultra-low frequency and broadband flexural wave attenuation using an inertant nonlinear metamaterial beam, Eng. Struct., vol. 323, pp. 119169, 2025. DOI: 10.1016/j.engstruct.2024.119169.
[34] A.V. Amirkhizi, Continuous gradient and discretized layered designs for control of stress wave scattering, Mech. Mater., vol. 109, pp. 18–25, 2017. DOI: 10.1016/j.mechmat.2017.03.010.
[35] M.I. Hussein, and M.J. Frazier, Metadamping: an emergent phenomenon in dissipative metamaterials, J. Sound Vib., vol. 332, no. 20, pp. 4767–4774, 2013. DOI: 10.1016/j.jsv.2013.04.041.
[36] A. Aladwani, and M. Nouh, Mechanics of metadamping in flexural dissipative metamaterials: analysis and design in frequency and time domains, Int. J. Mech. Sci., vol. 173, pp. 105459, 2020. DOI: 10.1016/j.ijmecsci.2020.105459.
[37] R. Abedi, and A.V. Amirkhizi, Use of loss limit approach to zero in scattering-based parameter retrieval of elastic microstructured media, Int. J. Solids Struct., vol. 200-201, pp. 34–63, 2020. DOI: 10.1016/j.ijsolstr.2020.05.010.
[38] S.J. Mitchell, A. Pandolfi, and M. Ortiz, Metaconcrete: designed aggregates to enhance dynamic performance, J. Mech. Phys. Solids., vol. 65, pp. 69–81, 2014. DOI: 10.1016/j.jmps.2014.01.003.
[39] S. J. Mitchell, A. Pandolfi, M. Ortiz, Investigation of elastic wave transmission in a metaconcrete slab, Mech. Mater., vol. 91, pp. 295–303, 2015.
[40] B. Zhang, L. Miao, T. Geng, and J. Zhang, Study on multi-bandgap characteristics and low-frequency vibration reduction of phononic-like crystal metaconcrete wave impeding block, Mech. Adv. Mater. Struct., early access, pp. 1–20, 2025. DOI: 10.1080/15376494.2025.2492313.
[41] N. Contreras, X. Zhang, H. Hao, and F. Hernández, Application of elastic metamaterials/meta-structures in civil engineering: a review, Compos. Struct., vol. 327, pp. 117663, 2024. DOI: 10.1016/j.compstruct.2023.117663.
[42] Y. Zhou, L. Ye, and W. Chen, Impact mitigation performance of hybrid metamaterial with a low frequency bandgap, Int. J. Mech. Sci., vol. 213, pp. 106863, 2022. DOI: 10.1016/j.ijmecsci.2021.106863.
[43] R. Raj, M.J. Prajapati, J.-T. Tsai, A. Kumar, and J.-Y. Jeng, Design and additive manufacturing of novel hybrid lattice metamaterial for enhanced energy absorption and structural stability, Mater. Des., vol. 245, pp. 113268, 2024. DOI: 10.1016/j.matdes.2024.113268.
[44] F. Aghighi, J. Morris, and A.V. Amirkhizi, Low-frequency micro-structured mechanical metamaterials, Mech. Mater., vol. 130, pp. 65–75, 2019. DOI: 10.1016/j.mechmat.2018.12.008.
[45] B.K. Zimmerman, S.P. Grenley, A.M. Saunders, J. Lind, D.A. Quint, E.B. Herbold, I. Lopez, and M. Kumar, Solid face sheets enable lattice metamaterials to withstand high-amplitude impulsive loading without yielding, Int. J. Impact Eng., vol. 195, pp. 105130, 2025. DOI: 10.1016/j.ijimpeng.2024.105130.
[46] W. Wang, and A.V. Amirkhizi, Reduced order modeling of dynamic mechanical metamaterials for analysis of infinite and finite systems, J. Appl. Mech., vol. 90, no. 9, pp. 91009, 2023. DOI: 10.1115/1.4062888.
[47] J. Morris, W. Wang, T. Plaisted, C.J. Hansen, and A.V. Amirkhizi, Optimizing graded metamaterials via genetic algorithm to control energy transmission, Int. J. Mech. Sci., vol. 263, pp. 108775, 2024. DOI: 10.1016/j.ijmecsci.2023.108775.
[48] L. GmbH, "Material Overview – LithaLox® HP 500 (Alumina)," Lithoz GmbH, Vienna, Austria, Technical Data Sheet, Dec., 2024. Accessed 9 June 2025. [Online]. Available https://www.lithoz.com/wp-content/uploads/2024/12/Lithoz_Materialfolder_EN_WEB.pdf
[49] COMSOL AB, Material Library User's Guide, 6th ed., COMSOL AB, Burlington, MA, 2024. accessed 9 June 2025. [Online]. Available: https://doc.comsol.com/6.2/doc/com.comsol.help.matlib/MaterialLibraryUsersGuide.pdf.
[50] J.O. Hallquist, Ed., LS-DYNA: Theory Manual. Livermore, California: Livermore Software Technology Corp, 2006.
[51] "LASSO Python Library, LASSO GmbH," accessed August 31, 2023. [Online]. Available: https://github.com/open-lasso-python/lasso-python
[52] C. Diez, qd—build your own ls-dyna tools quickly in Python. In 15th International LS-DYNA Users Conference, Detroit, MI, USA, 2018.

[53] W. Quach, J. Teng, and K.F. Chung, Residual stresses in steel sheets due to coiling and uncoiling: a closed-form analytical solution, Eng. Struct., vol. 26, no. 9, pp. 1249–1259, 2004. DOI: 10.1016/j.engstruct.2004.04.005.

[54] M.I. Rosa, B.L. Davis, L. Liu, M. Ruzzene, and M.I. Hussein, Material vs. structure: topological origins of band-gap truncation resonances in periodic structures, Phys. Rev. Mater., vol. 7, no. 12, pp. 124201, 2023. DOI: 10.1103/physrevmaterials.7.124201.

[55] C. Sugino, Y. Xia, S. Leadenham, M. Ruzzene, and A. Erturk, A general theory for bandgap estimation in locally resonant metastructures, J. Sound Vib., vol. 406, pp. 104–123, 2017. DOI: 10.1016/j.jsv.2017.06.004.

[56] S. Kumar, and M. Kumar, Damping implementation issues for in-structure response estimation of seismically isolated nuclear structures, Earthq. Engng. Struct. Dyn., vol. 50, no. 7, pp. 1967–1988, 2021. DOI: 10.1002/eqe.3436.

[57] L.-D. Lstc, Keyword User's Manual (Version 971 r6. 0.0), Livermore Software Technology Corporation, Livermore, CA, USA, 2012.

[58] B. Liu, S. Yang, W. Li, and M. Zhang, Damping dissipation properties of rubberized concrete and its application in anti-collision of bridge piers, Constr. Build. Mater., vol. 236, pp. 117286, 2020. DOI: 10.1016/j.conbuildmat.2019.117286.

[59] K. Lambrinou, T. Lauwagie, F. Chalvet, G. De Portu, N. Tassini, S. Patsias, T. Lube, and O. Van der Biest, Elastic properties and damping behaviour of alumina–alumina/zirconia laminates, J. Eur. Ceram. Soc., vol. 27, no. 2–3, pp. 1307–1311, 2007. DOI: 10.1016/j.jeurceramsoc.2006.04.124.

[60] T.J. Hughes, The Finite Element Method: Linear Static and Dynamic Finite Element Analysis. Mineola, NY, USA: Courier Corporation, 2003.

[61] S. Panteliou, K. Zonios, I. Chondrou, H. Fernandes, S. Agathopoulos, and J. Ferreira, Damping associated with porosity in alumina, Int. J. Mech. Mater. Des., vol. 5, no. 2, pp. 167–174, 2009. DOI: 10.1007/s10999-008-9092-0.

[62] R.W. Clough and J. Penzien, Dynamics of Structures. New York, NY, USA: McGraw-Hill, 1993.

[63] H. Koruk, and S. Rajagopal, A comprehensive review on the viscoelastic parameters used for engineering materials, including soft materials, and the relationships between different damping parameters, Sensors, vol. 24, no. 18, pp. 6137, 2024. DOI: 10.3390/s24186137.

[64] B. Zhou, and X. Zhang, Comparison of five viscoelastic models for estimating viscoelastic parameters using ultrasound shear wave elastography, J. Mech. Behav. Biomed. Mater., vol. 85, pp. 109–116, 2018. DOI: 10.1016/j.jmbbm.2018.05.041.

[65] W. Wang, W. Cheney, and A.V. Amirkhizi, Generative design of graded metamaterial arrays for dynamic response modulation, Mater. Des., vol. 237, pp. 112550, 2024. DOI: 10.1016/j.matdes.2023.112550.